Electronic Supplementary Information (ESI)

Effect of pore mesostructure on the electrooxidation of glycerol by Pt mesoporous catalysts

Athira Anil,[a] Jai White,[b] Egon Campos dos Santos,[c] Irina Terekhina,[d] Mats Johnsson,[d] Lars G.M. Pettersson [e], Ann Cornell,[b] and German Salazar Alvarez[a*]

a.   *Department of Material Science and Engineering, Ångström Laboratory, Uppsala University, Box 35 751 03 Uppsala, Sweden*
b.   *Department of Chemical Engineering and Technology, KTH Royal Institute of Technology, Stockholm 114 28, Sweden*
c.   *Advanced Institute of Materials Research (WPI-AIMR), Tohoku University, Sendai 980-8577, Japan*
d.   *Department of Materials and Environmental Chemistry, Arrhenius Laboratory, Stockholm University, Stockholm106 91, Sweden*
e.   *Department of Physics, Stockholm University, Stockholm 106 91, Sweden*

Table of Contents

1. Experimental details

1.1. Pre-treatment of substrate

The as-purchased nickel foils of thickness 0.125 mm were sonicated in 3 M HCl for 3 h to improve the surface roughness of the material. Our experiments observed that the surface roughed surfaces show better adhesion to the deposited platinum than nickel foils purchased.

1.2. Synthesis of mesoporous catalysts

The HPC catalysts were synthesized using electrodeposition technique at -0.4 vs. Ag/AgCl in an aqueous solution 100 mM hexachloroplatinic acid, 200 mM H_3BO_3, 25 mM NH_4Cl, and 1 wt% of pluronic F-127[1]. All the chemicals are purchased from Sigma Aldrich and used without purification. The pH of the solution was adjusted between 2.5 -3 using HCl. Boric acid maintains pH buffer,[2] whereas pluronic F-127 was used as the template. Cubic pores and linear pores catalyst (CPC & LPC) were synthesized using phytantriol templating adapted from previous reports:[3–5] A three-electrode electrochemical cell with 50 ml volume with platinum mesh counter electrode, Ag/AgCl reference electrode, and pre-treated 0.5 cm^2 nickel substrate is used for electrodeposition. Hexachloroplatinic acid, phytantriol, and 0.12 mm thick nickel substrate were purchased from Sigma Aldrich and used as received without any purification. The CPC and LPC are synthesized by dip-coating a Ni substrate in phytantriol, followed by 100 mM platinic acid infiltration for 1 h. The as-infiltrated Pt was potentiostatically electrodeposited on to the substrate using a potential of -250 mV vs. Ag/AgCl. The infiltration and deposition temperature for CPC and LPC were maintained at 25 °C and 50 °C respectively. The template was further removed by washing the deposited substrate on ethanol.

1.3. Material characterization

The mesoporous thin films were characterized using microscopic, spectroscopic, and diffractometric tools. A Bruker D5000 *θ-2θ* parallel beam diffractometer with a Cu microfocus X-ray source (λ=1.54 Å) and a charge coupled device (CCD) detector was used to study the crystalline quality of the mesoporous thin films in Grazing Incidence X-ray Diffractometer (GIXRD) mode. X-ray Photoelectron Spectroscopy (XPS) measurements were carried out using a physical electronics Quantera 2 XPS with

monochromatic Al operated at 15 kV with a total power of 50 W and a spot size of 100 μm. The base pressure in the measurement chamber was maintained at about 7×10^{-10} bar. Four different regions in the sample were selected for the survey scan examined. Similar results from all the selected regions demonstrate the film's uniformity. The survey was obtained in quintuplicate in the region 0-1040 eV, using a pass energy of 224 eV and a step size of 0.1 eV. High-resolution spectra were acquired using 26 eV pass energy spectra and a 0.05 eV resolution.

1.4. Electrochemical cell set up

All electrochemical experiments were undertaken in a 10 mL divided cell in which 5 mL of the respective electrolyte was taken for each study in each compartment. The working electrodes (Pt-based catalysts on Ni foil) were held using a stainless-steel electrode holder adjacent to a Luggin capillary with a Hg/HgO (1 M NaOH) reference electrode in the anode compartment. In the cathode compartment, the counter electrode was a Pt grid. Hg/HgO (1.0 M NaOH) is used as reference electrode and the conversion to reversible hydrogen electrode (RHE) is done using

$$E_{RHE} = E_{Hg/HgO}^{Ref} + E_{Hg/HgO}^{M} + (0.0591 \times pH_{)}.$$

1.5. Electrochemical surface area, ECSA

To measure ECSA, solutions of N_2-saturated 0.1 M NaOH and a Nafion 212 membrane were used at ambient temperature (22 – 24 °C). In addition, cyclic voltammetry in the potential window -0.863 to -0.338 V vs. Hg/HgO (1.0 M NaOH) at a scan rate of 50 $mV \cdot s^{-1}$ (see figure S1a) was undertaken, and the area of the oxidation (desorption) peaks was discerned (see table in figure S1c). A specific charge of 210 $\mu C \cdot cm^{-2}$ was used for the polycrystalline Pt electrocatalysts.[6,7] The electrochemical surface area (ECSA) was determined by calculating the Coulombic charge passed from the hydrogen underpotential deposition (HUPD) due to the adsorption and desorption of H atoms at the catalyst surface.[6,7] The ECSA of the mesoporous catalysts and the commercial catalyst Pt/C calculated by integrating HUPD curves are shown in Figure S1a from 0.1 to 0.45 V vs RHE. The hydrogen absorption and desorption peaks are more evident in commercial Pt/C and CPC compared to HPC and LPC which is also reflected in calculated ECSA. The ECSA of the studied systems are CPC (55.6 cm^2) > Pt/C (26 cm^2) HPC > (14.4 cm^2) > LPC (10.6 cm^2).
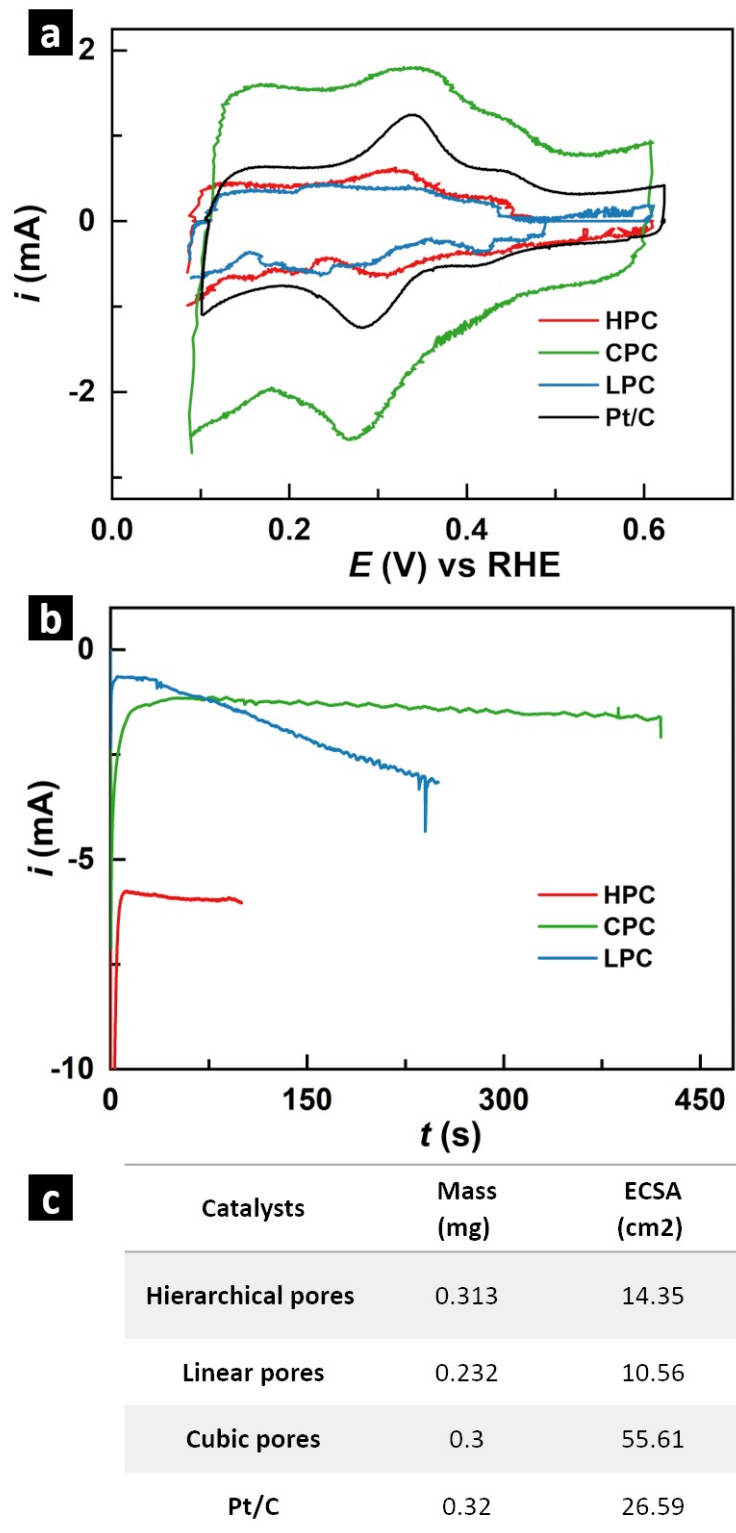
Figure S1: (a) HUPD curves of mesoporous catalysts that are used for ECSA calculations, (b) deposition current vs time during the potentiostatic electrodeposition of Pt in each mesoporous system, (c) Mass deposited and ECSA of each catalyst calculated from the figure S1a and figure S1b. All the CV were carried out at a scan rate of 50 mV·s^{-1} in 1 M NaOH solution.
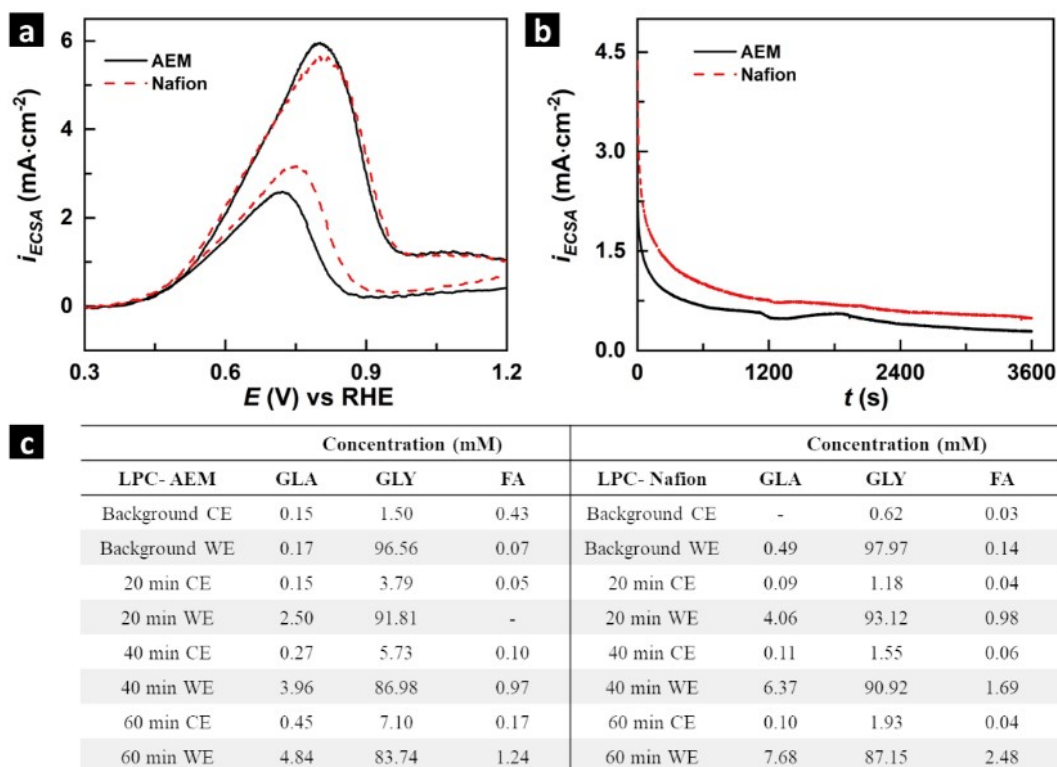
1.6. Glycerol electrooxidation
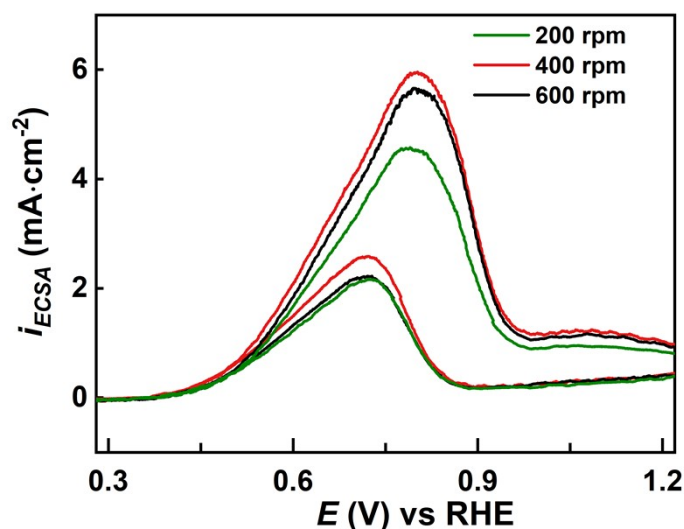
Figure S2: Glycerol electrooxidation studies in 0.1 M glycerol + 1 M NaOH on linear pores with different stirrer rates.

A N_2-saturated 1 M of NaOH and 0.1 M of glycerol solution at 60 °C was used to study the GEOR in the setup described above. A Nafion 212 membrane and FuMA-Tech Fumasep FAA-3-50 alkaline exchange membrane (F-AEM) were used (both with thicknesses of approximately 50 μm) to compare which membrane provided the best performance and the least amount of crossover. We measured CV at different rotation rates (200, 400, and 600 rpm) to optimize the stirrer bar rotation rate. It can be seen in figure S2a that 400 rpm provides the highest peak current density compared to a lower and higher RPM of 200 and 600, and thus, 400 rpm was used in the anodic compartment for all experiments. The LPC was used to analyse the effect of the membrane in the divided cell. This was done to study both the effect on the glycerol electrooxidation reaction (GEOR) performance (see figure S3a & S3b) and glycerol and glycerol oxidation product crossover from the anode compartment to the cathode compartment (see table in figure S3c). Figure S3a shows that the peak current density for the alkaline exchange and Nafion membrane was approximately 5.70 mA·cm^{-2} and 5.50 mA·cm^{-2}. Table S3c shows that at every interval at which a 100 μL sample was taken from the cathode compartment in the study of the alkaline exchange membrane and Nafion membranes, there was a more significant concentration of glycerol in the alkaline

exchange membrane. This indicates a higher amount of crossover. As a result of Nafion having an approximately equal performance for the Pt linear pores but a minor crossover, it was used for the ongoing experiments to compare the different structures for the performance and glycerol oxidation products analysis via HPLC.

LPC- AEM	Concentration (mM)			LPC- Nafion	Concentration (mM)		
	GLA	GLY	FA		GLA	GLY	FA
Background CE	0.15	1.50	0.43	Background CE	-	0.62	0.03
Background WE	0.17	96.56	0.07	Background WE	0.49	97.97	0.14
20 min CE	0.15	3.79	0.05	20 min CE	0.09	1.18	0.04
20 min WE	2.50	91.81	-	20 min WE	4.06	93.12	0.98
40 min CE	0.27	5.73	0.10	40 min CE	0.11	1.55	0.06
40 min WE	3.96	86.98	0.97	40 min WE	6.37	90.92	1.69
60 min CE	0.45	7.10	0.17	60 min CE	0.10	1.93	0.04
60 min WE	4.84	83.74	1.24	60 min WE	7.68	87.15	2.48

Figure S3: (a) Comparison of alkaline exchange membrane (AEM) and Nafion on glycerol electrooxidation with 0.1 M glycerol + 1 M NaOH at scan rate 10 mV·s⁻¹ at 60 °C. (b) Chronoamperometric curves at constant potential 0.69 V vs RHE. (c) HPLC catalysis of GO products of LPC catalyst electrolysed at AEM and Nafion membranes.
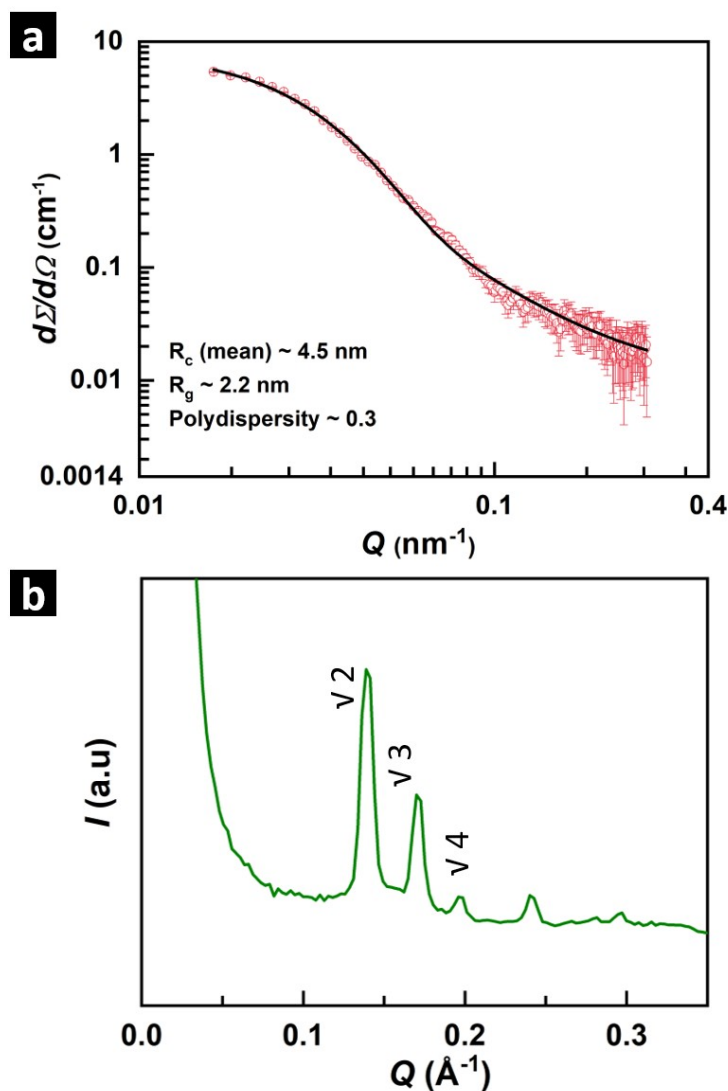
Figure S4: (a) SANS data of the 1 *wt*% pluronic acid micelles in water. (b) SAXS data of cubic crystal phase of phytantriol.

1.7. Characterization of templates

Figure S4 a represents the small angle neutron scattering (SANS) pattern of pluronic F127 micelles formed in the electrolyte solution. [8] The micelles of F127 (1 *wt*%) are modelled using the form factor *P(Q)* as described in Pedersen et al. [9] considering that the micelles of F127 block polymer consist of a spherical core of hydrophobic chains (PPO) with a corona of hydrophilic chains (PEO).[10] The core radius is found to be around 4.5 nm, while the radius of gyration of the PEO blocks is found at 2.2 nm. forms micelles above the critical micellar concentration[11] which deposit on the cathode templating the deposition of platinum.[8,12]

The small angle X-ray scattering (SAXS) of Q224 of phytantriol at room temperature shows four distinct reflections with relative positions of 1/d in ratios $\sqrt{2}:\sqrt{3}:\sqrt{4}:\sqrt{6}$, which can be

indexed to (*hkl*) = (110), (111), (200) and (211) reflections of a cubic lattice of crystallographic space group *Pn3m* (Q224)[4,5]

1.7.1. Theoretical details of SANS

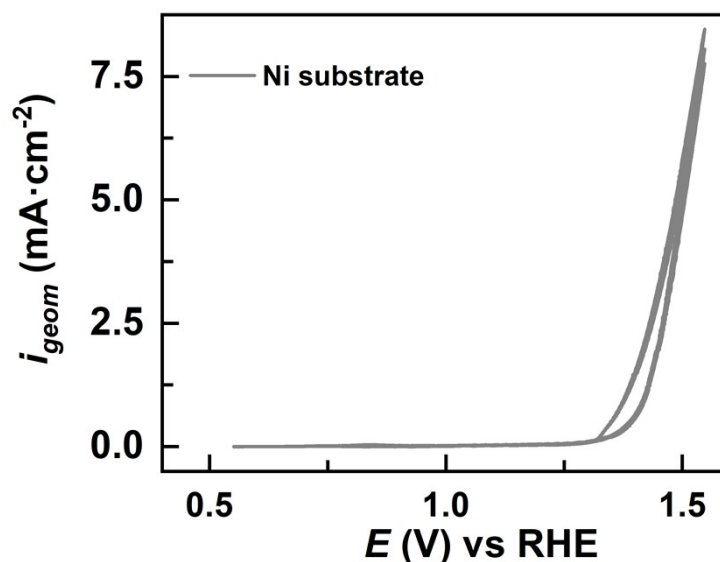For polydispersed systems, $d\Sigma/d\Omega$ in equation (2) is modified as:

$$\frac{d\Sigma}{d\Omega}(Q) = \int \frac{d\Sigma}{d\Omega}(Q,R) f(R) dR + B \qquad (S1)$$

where *f(R)* is the size distribution and usually accounted by log normal distribution as given by

$$f(R) = \frac{1}{R\sigma\sqrt{2\pi}} \exp\left[-\frac{\left(\ln \frac{R}{R_{med}}\right)^2}{2\sigma^2} \right] \qquad (S2)$$
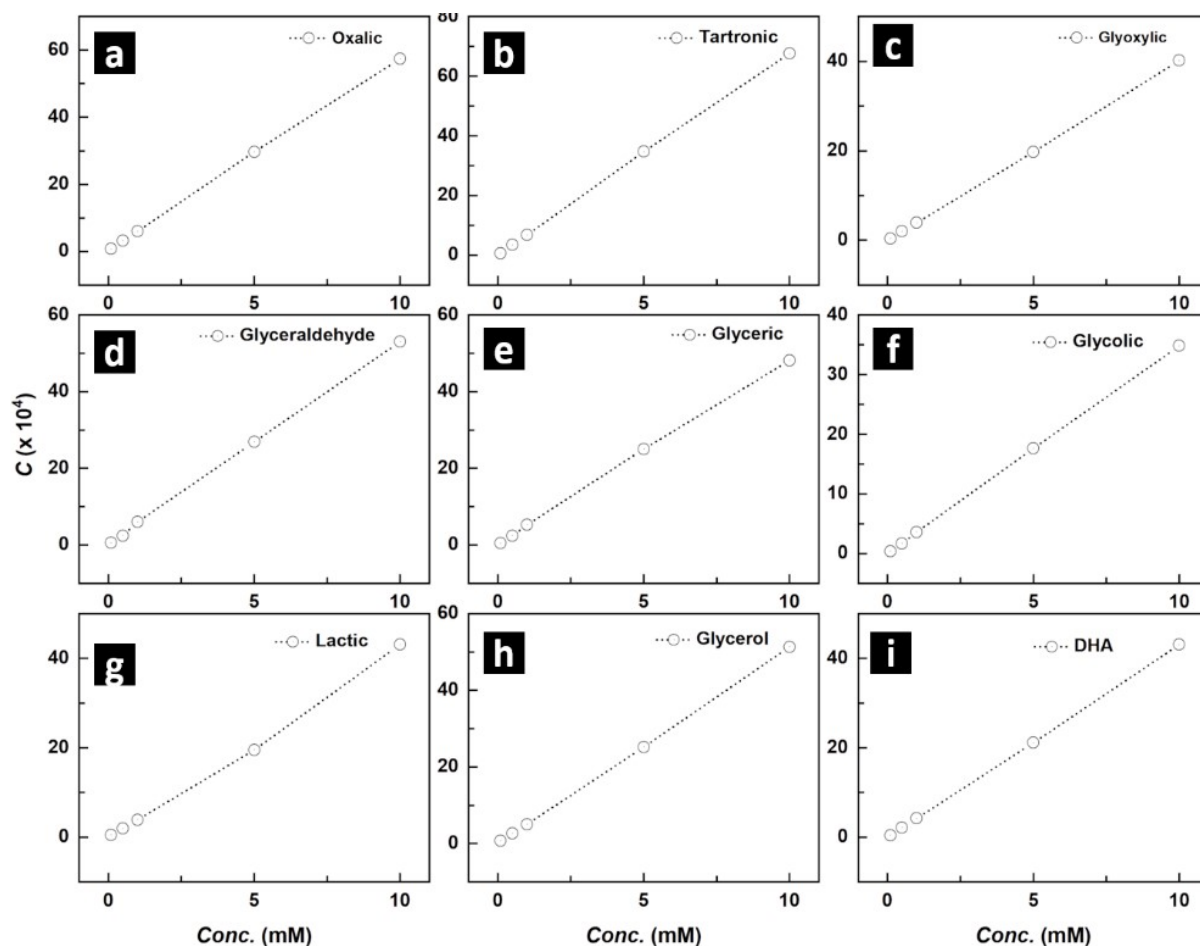
where R_{med} and σ are the median value and standard deviation, respectively. The mean (R_m) and median values are related as $R_m = R_{med} \exp(\sigma^2/2)$.

1.8. Electrochemical studies of Ni substrate

Figure S5: CV of Ni RDE at 60 °C. Experiment is carried out in 0.1 M glycerol + 1 M NaOH at scan rate 10 mV·s^{-1} at 500 rpm.

1.9. Oxidation product analysis

Figure S6: HPLC calibration plots of (a) Oxalic acid (OA), (b) Tartronic acid (TA), (c) Glyoxylic acid , (d) Glyceraldehyde, (e) Glyceric acid (GLA), (f) Glycolic acid (GA), (g) Lactic acid (LA), (g) Glycerol, (i) Dihydroxy acetone (DHA).
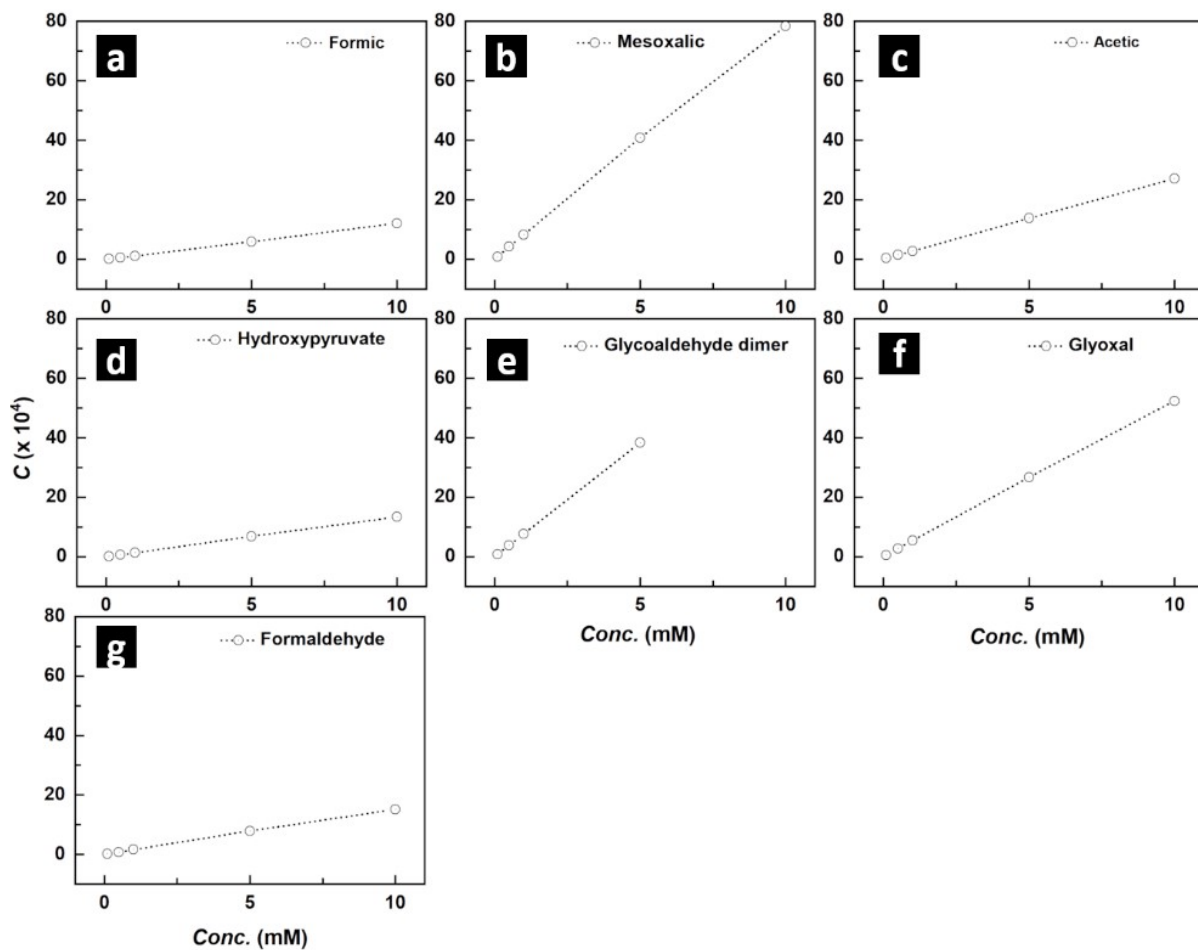
Figure S7: HPLC calibration plots for(a) Formic acid (FA), (b) Mesoxalic acid, (c) Acetic acid (AA), (d) Hydroxy pyruvate (HDP), (e) Glycolaldehyde dimer, (f) Glyoxal, (g) Formaldehyde.

2. Additional Results

2.1. Grazing incidence X-ray diffraction, GIXRD
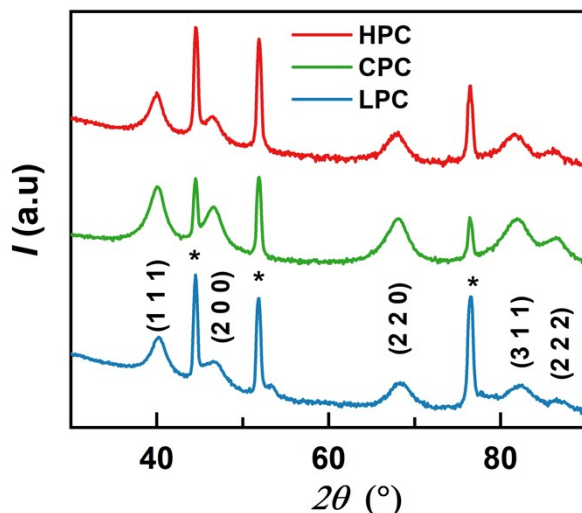
Figure S8: GIXRD of pristine HPC, CPC and LPC deposited on nickel substrate. * indicates the diffraction peaks of the Ni substrate.

GIXRD measurements are shown in figure S8. All the three different types of mesoporous thin-film catalysts show (111), (200), (220), (311), and (222) reflections that correspond to the polycrystalline platinum with the fcc unit cell.[13] The HPC, CPC, and LPC lattice parameter was calculated using the Braggs law and found to be 0.390 nm, 0.389 nm, and 0.389 nm, respectively. A slight contraction of the platinum lattice is observed in all three thin films compared to pure platinum (a = 0.392 nm). The compressive strain induced on the platinum atoms upon electrodeposition on a metal substrate with smaller lattice constant could be the reason.[14,15] The GIXRD peaks observed at 44.48 °, 51.80 °, and 76.42 ° correspond to the (111), (200) and (220) planes of nickel substrate.[16]

2.2. Xray-Photoelectron Spectroscopy

Figure S6 shows the XPS spectrum of the pristine mesoporous catalysts. The XPS $4f$ spectra of all the catalysts show doublet peaks at 71.3 eV and 74.7 eV, each of which can be further deconvoluted into three different peaks corresponding to Pt^0, Pt^{II}, and Pt^{IV}

oxidation states.[17,18] The integrated area of the deconvoluted peaks was quantified, and
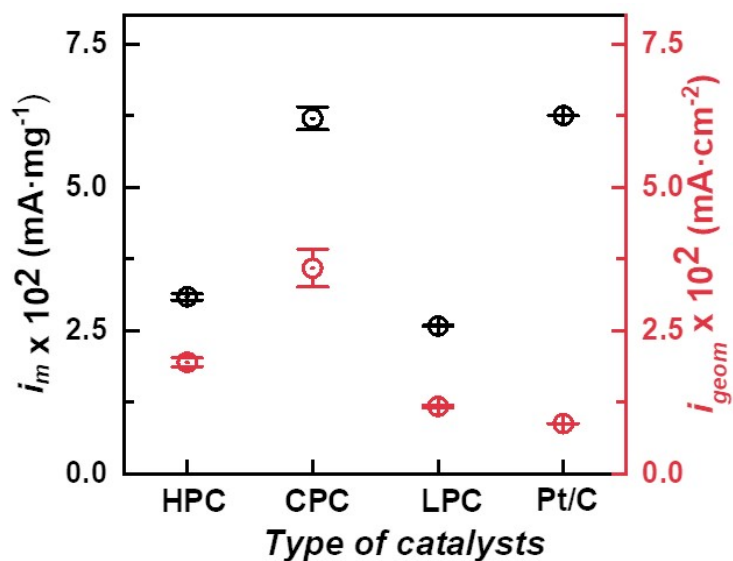
the ratio of metallic platinum to the platinum oxides ($PtO + PtO_2$) follows the ratio, LPC (1.33) > HPC (1.32) > CPC (1.30) respectively for each of the catalysts. Thus, the catalytic surface mainly consists of metallic Pt atoms, and fewer platinum oxides are
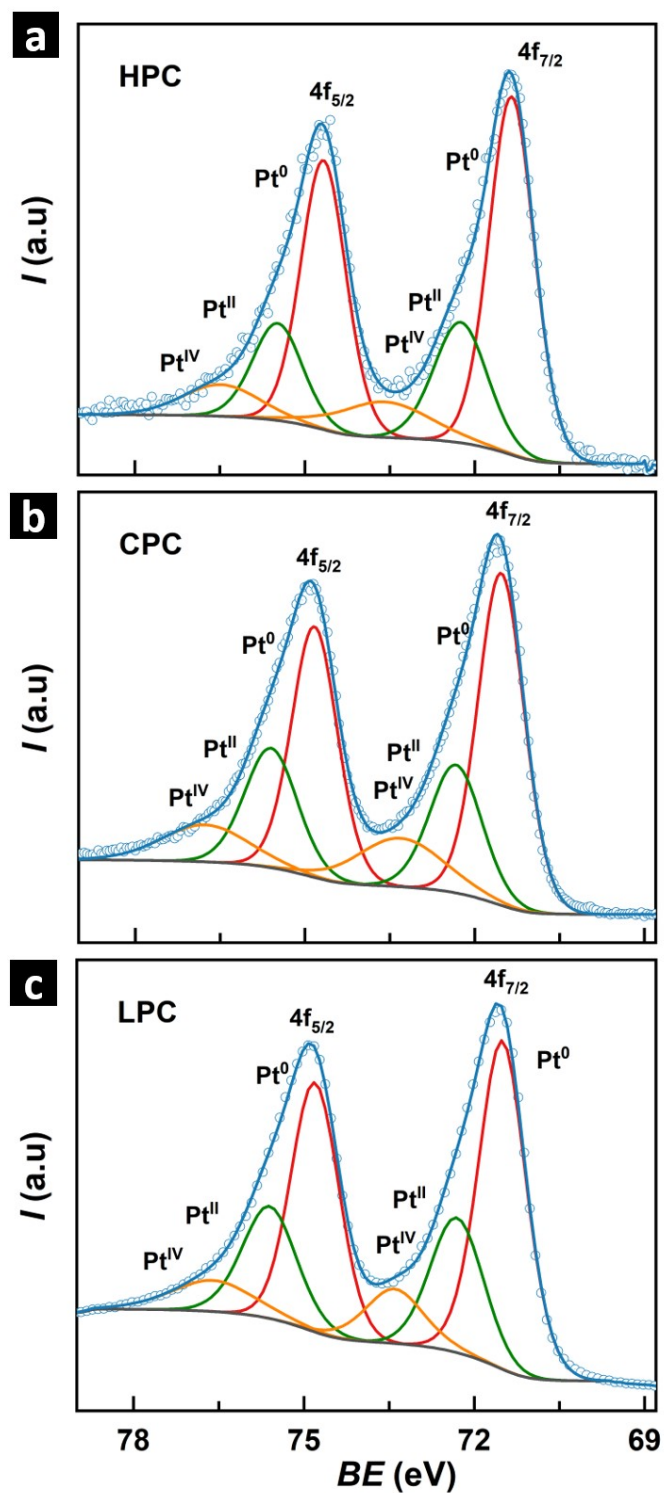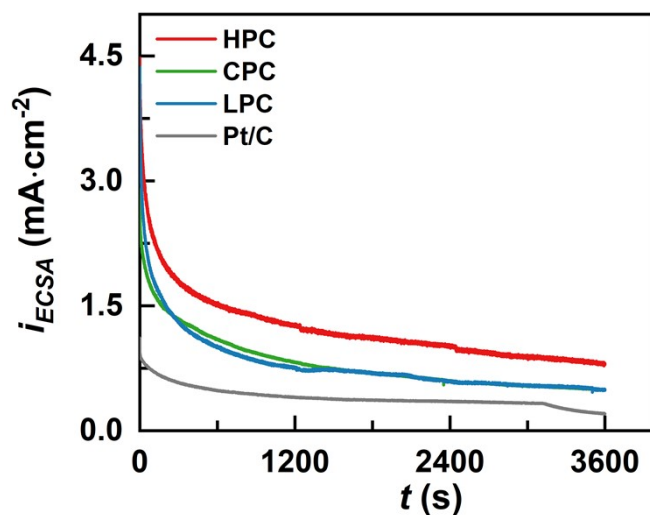

also present.

Figure S9: XPS studies of pristine (a) HPC, CPC, and LPC, respectively.

2.3. Mass activity and geometric activity

Figure S10: Mass activities, i_m (black), and geometrical current densities, i_g (red) of HPC, CPC, LPC and Pt/C catalysts at scan rate 10 mV·s^{-1} at 60 °C. All the experiments were carried out with stirring at 400 rpm.

2.4. Chronoamperometric curves

Figure S11: Chronoamperometric curves, (i_{ESCA} vs t) of HPC, CPC, LPC and Pt/C catalysts at applied potential of 0.69 V vs RHE at 60 °C. All the experiments were carried out with stirring at 400 rpm.

2.5. Tafel slopes
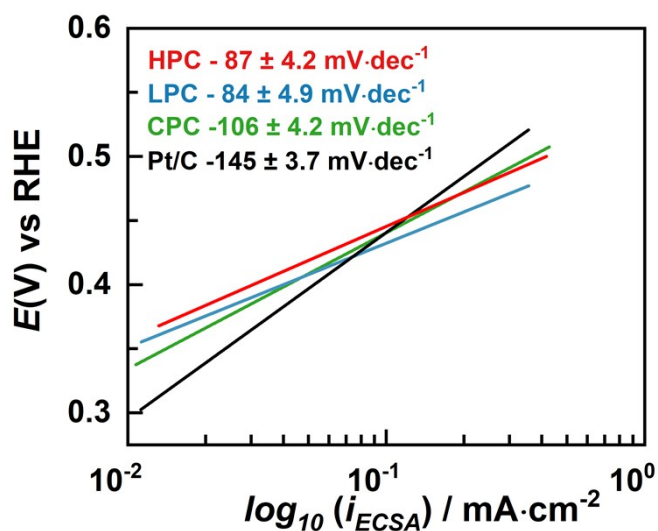
Figure S12: Electrochemical studies of mesoporous catalysts at 60 °C: Tafel slope of HPC, LPC, CPC and Pt/C calculated from the polarization curves shown in Fig. 2b. All the experiments are carried out in 0.1 M glycerol + 1 M NaOH at scan rate 10 mV·s^{-1} at 400 rpm stirring rate.
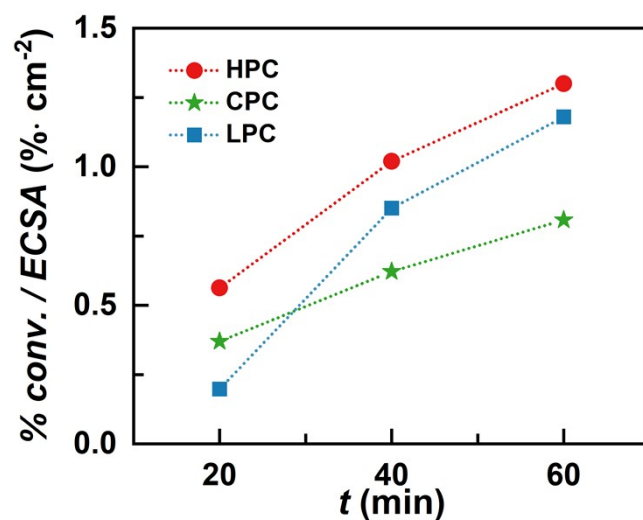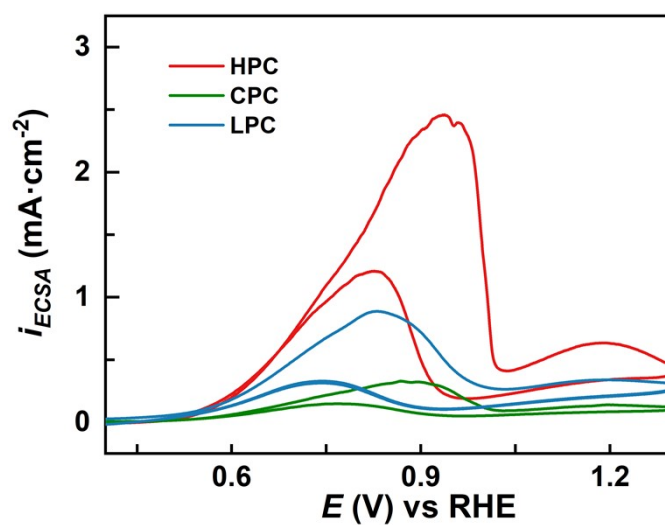

2.6. Glycerol conversion rate

Figure S13: Glycerol conversion percentages per ECSA of mesoporous catalysts at 60 °C. All the experiments are carried out in 0.1 M glycerol + 1 M NaOH at scan rate 10 mV·s^{-1} at 400 rpm stirring rate.

2.7. Electrochemical performance at room temperature

Figure S14: Electrochemical studies of mesoporous catalysts at 25 °C: CV of HPC, CPC, and LPC. All the experiments are carried out in 0.1 M glycerol + 1 M NaOH at scan rate 10 mV·s^{-1} at 400 rpm stirring rate.

3. Comparison with the literature

Table S1: Comparison of electrochemical performance of the present mesoporous catalysts and previously reported values.

Catalyst	Electrolyte	Scan rate (mV·s^{-1})	i_{ECSA} (mA·cm^{-2})	Ref.
HPC	0.1 M Gly + 1 M NaOH	10	6.94	This work
CPC	0.1 M Gly + 1 M NaOH	10	3.26	This work
LPC	0.1 M Gly + 1 M NaOH	10	5.62	This work
Pt/C (20 wt%) Commercial catalyst	0.1 M Gly + 1 M NaOH	10	1.63	This work
Pt nanostructured	0.1 M Gly + 1 M NaOH	10	1.25	[19]
Pt supported on C	1 M Gly + 1 M KOH	50	3.00	[20]
Pt black	0.5 M Gly + 0.5 M KOH	50	2.50	[21]
ALD-TiO2 – Pt/C (HT)	2 M Gly + 0.5 M H$_2$SO$_4$	50	0.23	[22]
ALD-TiO2 – Pt/C	2 M Gly + 0.5 M H$_2$SO$_4$	50	0.21	[22]

Table S2: Typical oxidation products reported in the literature. All the potentials are represented with respect to RHE and all variables are at 60 °C except *.

Catalyst	Electrolyte	T (°C)	E (V) / t (h)	f %							Ref.
				GLA	TTA	GD	DHA	OA	FA	GA	
HPC	0.1 M Gly + 1 M NaOH	60	0.69/ 1	59	10	0	0	6	18		This work
CPC	0.1 M Gly + 1 M NaOH	60	0.69/ 1	58	5	0	0	14	14		This work
LPC	0.1 M Gly + 1 M NaOH	60	0.69/ 1	60	7	0	0	2	17		This work
Pt/GNS	0.5 M Gly+ 0.5 M KOH	60	0.67/ 2	~16	~2	~31	-	~11	-	~37	[23]
Pt/C	1 M Gly + 2 M KOH	60	0.73/ 2	41	40	-	-	-	-	18	[24]
Pt/C (20 wt%)	1 M Gly + 4 M KOH	60		~7	~72	-	-	~18	-	~3	[25]
Pt/C (40 wt%)	1 M Gly + 4 M KOH	60		~13	~67	-	-	~15	-	~5	[25]
Pt/C (60 wt%)	1 M Gly + 4 M KOH	60		~12	~64	-	-	~25		~3	[25]
*Pt/CNT	0.5 M Gly + 0.5 M KOH	-	0.72/ 2.5		~75	~1	-	~3		-	[26]
*Pt/C (40 wt%)	0.5 M Gly + 0.5 M KOH	RT	0.7/ -	~4	-	~13	~45	~6		~20	[27]
Pt - VGCC	0.1 M Gly + 1 M KOH	60	0.83/2	47	3	-	20	7	0	23	[28]
Pt nanoparticles	0.1 M Gly + 1 M KOH	25	0.8/1	76	3	0	0	4	9	5	[29]
Pt/C	0.1 M Gly + 1 M KOH	25	0.8/1	73	14	0	0		7	4	[29]

4. Computational methods

4.1. Computational details

Adsorption energies of glycerol intermediates were calculated for Pt(111) and Pt(100) surfaces. The models of the catalytic surfaces (see Figure S15) were constructed using the Atomic simulation environment (ASE).[30] The calculations were carried out on a (4×4×4) slab with a vacuum of 20 Å to avoid interactions between periodic images. The structures were optimized to energy and atom force convergence criteria of 10^{-5} eV and 0.01 eV·Å^{-1}, respectively. The bottom two atomic layers of the slab were kept fixed. From the pre-optimized surfaces, intermediates were placed above the topmost atoms and re-optimized. All calculations were performed using Density functional theory (DFT) as implemented in the Vienna ab initio simulation package (VASP).[31] The exchange-correlation functional was approximated as the Bayesian Error Estimation Functional (BEEF-vdW)[32] with an additional nonlocal correlation term. Khon-Shan equations were solved using the projected augmented wave (PAW)[33,34] method to describe the ionic cores, whereas the valence electrons were treated by plane-wave basis set with a cutoff of 450 eV. Brillouin-zone sample was performed in a reciprocal grid with a space resolution of $2\pi \times 0.04$ Å^{-1}, here equivalent to a Monkhorst-Pack 4×4×1 k-point mesh. The Methfessel-PaxtonField approach with a gaussian width of 0.2 eV was employed for all systems, and all energies were extrapolated to $T = 0$ K.

The adsorption free energies ($\Delta G_{C_xH_yO_z}$) of the intermediates ($C_xH_yO_z$) in the reaction were referenced with respect to the gas phase energies of H_2, H_2O and CH_4 molecules. $\Delta G_{C_xH_yO_z}$ is defined as:

$$\Delta G_{C_xH_yO_z} = G_{slab + C_xH_yO_z} - G_{slab} - x\left(G_{CH_4} - 2G_{H_2}\right) - \frac{y}{2}G_{H_2} - z\left(G_{H_2O} - G_{H_2}\right), \qquad (S3)$$

where $G_{slab + C_xH_yO_z}$, G_{slab}, G_{CH_4}, G_{H_2O}, and G_{H_2} are the energies of the adsorbed intermediate, pure slab, CH_4 molecule, H_2O molecule, and H_2 molecule, respectively. x, y, and z represent the molecule's number of carbon, hydrogen, and oxygen atoms. To obtain reaction free energies, DFT total energies were corrected by zero-point energies (ZPE) and thermal contributions of the reference compounds. The harmonic approximation was employed for the vibrational frequency calculations, and all vibrational modes of the adsorbates and molecules were calculated. Henry's law was

used to link the gas phase pressure to the aqueous concentration using constants obtained from the NIST-JANAF[35] tables. A concentration of 0.1 mol·L^{-1} was used for glycerol, and the temperature was set to 298 K. The electrochemical environment was modelled based on the computational hydrogen electrode.[36] The free energy of a proton-electron pair (H$^+$ + e$^-$) is determined as: $1/2G_{H_{2(g)}} - eU_{RHE}$, where $G_{H_{2(g)}}$ is the free energy of the hydrogen at standard conditions, and U_{RHE} the potential against the reversible hydrogen electrode. Solvation effects were considered using an implicit solvent correction[37,38] implemented in VASP.[31] We note that it is necessary to include explicit water to entirely obtain the solvation effect on the electrochemical interface. However, we have previously shown that implicit solvation can describe electrode/electrolyte interfaces with reasonable accuracy.[11] Thus, we choose to use implicit solvent correction that partially captures the effect of the solvation energies. Reaction energetics including thermodynamics corrections are shown in an Excel file in Supplementary Material.
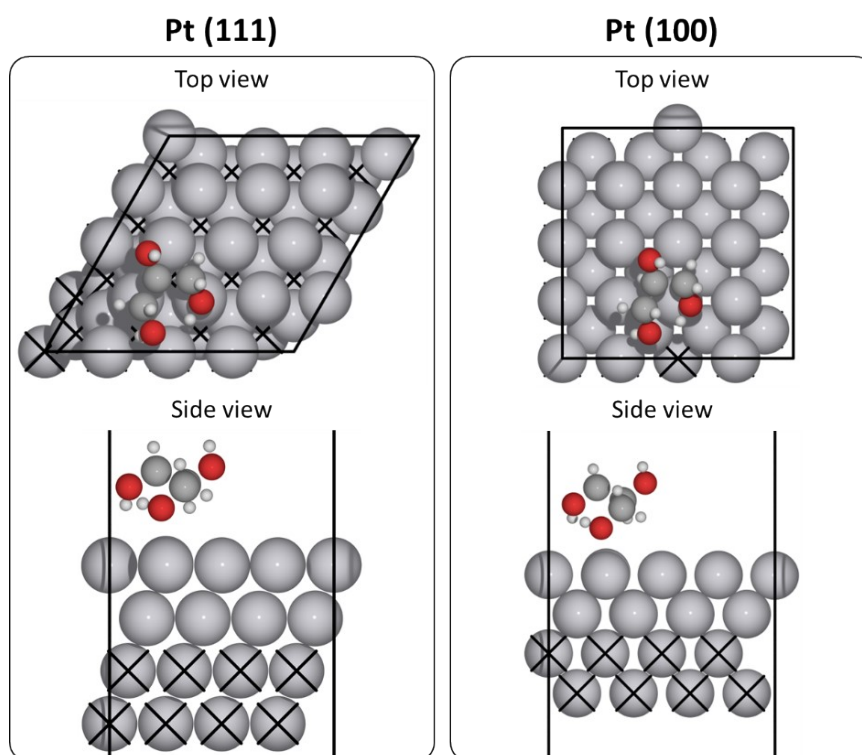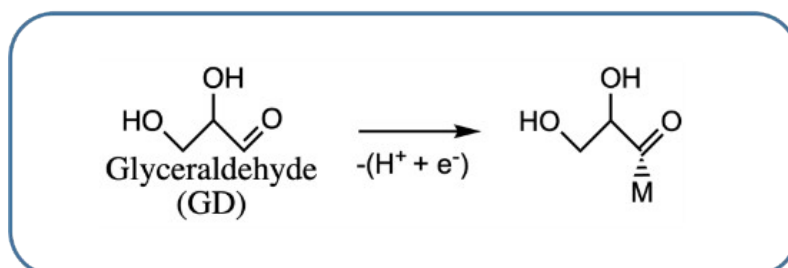

Figure S15: Slab models used to calculate adsorption energies. (left) and (right) show glycerol adsorption on Pt (111) and Pt (100), respectively. The two bottom layers were fixed during structure optimization.

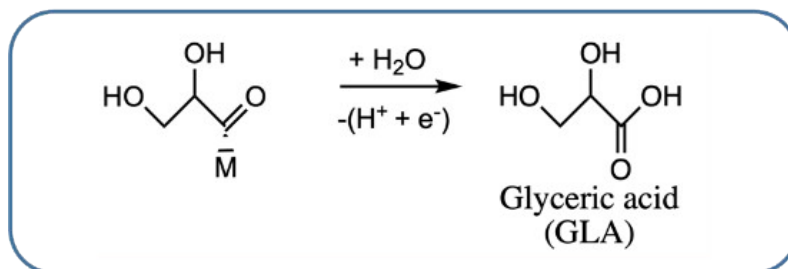### 4.2. Calculated free energies and reaction intermediates

As indicated in Figure S16, glycerol oxidation reactions can be classified into three groups: deprotonation, hydrolysis, and hydrogen rearrangement. In the deprotonation reaction, a reaction intermediary ($C_xH_yO_z$) loses a proton, and an electron forming chemical bonds with the closest reactive site (M) on the surface. In the hydrolysis, water reacts with the carbonyl group attached to the surface, forming the carboxyl group. Hydrolysis reactions can occur in two different ways: 1) the water adsorbed on the surface loses a proton and then the hydroxyl reacts with the carbonyl group, 2) a concerted mechanism where the water molecule loses the proton, and at the same time the OH group react with the carbonyl. Finally, 3) hydrogen rearrangement occurs breaking carbon-carbon bonds.

Three assumptions have been considered to simulate glycerol oxidation reactions. First, all reactions take place in the vicinities of the electrode surface. Second, it will always have a site (M) available to react, thus forming M-O and M-C chemical bonds on the surface. Third, all the liquid products (indicated in figure 4) are formed on the electrode surface, and once the liquid product is formed, it moves to the electrolyte leaving the surface free to react.
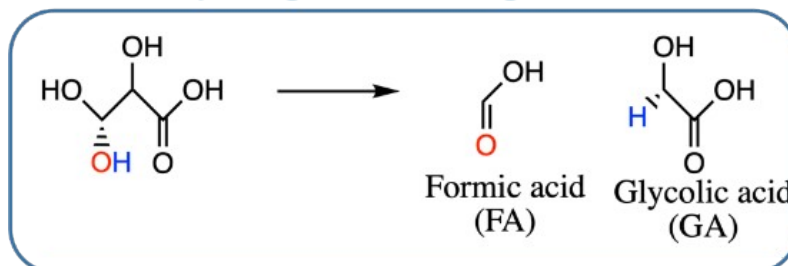
Figure S16: Examples of the three reactions considered in this work. All the elementary steps to obtain glycerol oxidation products are shown in the following figures.
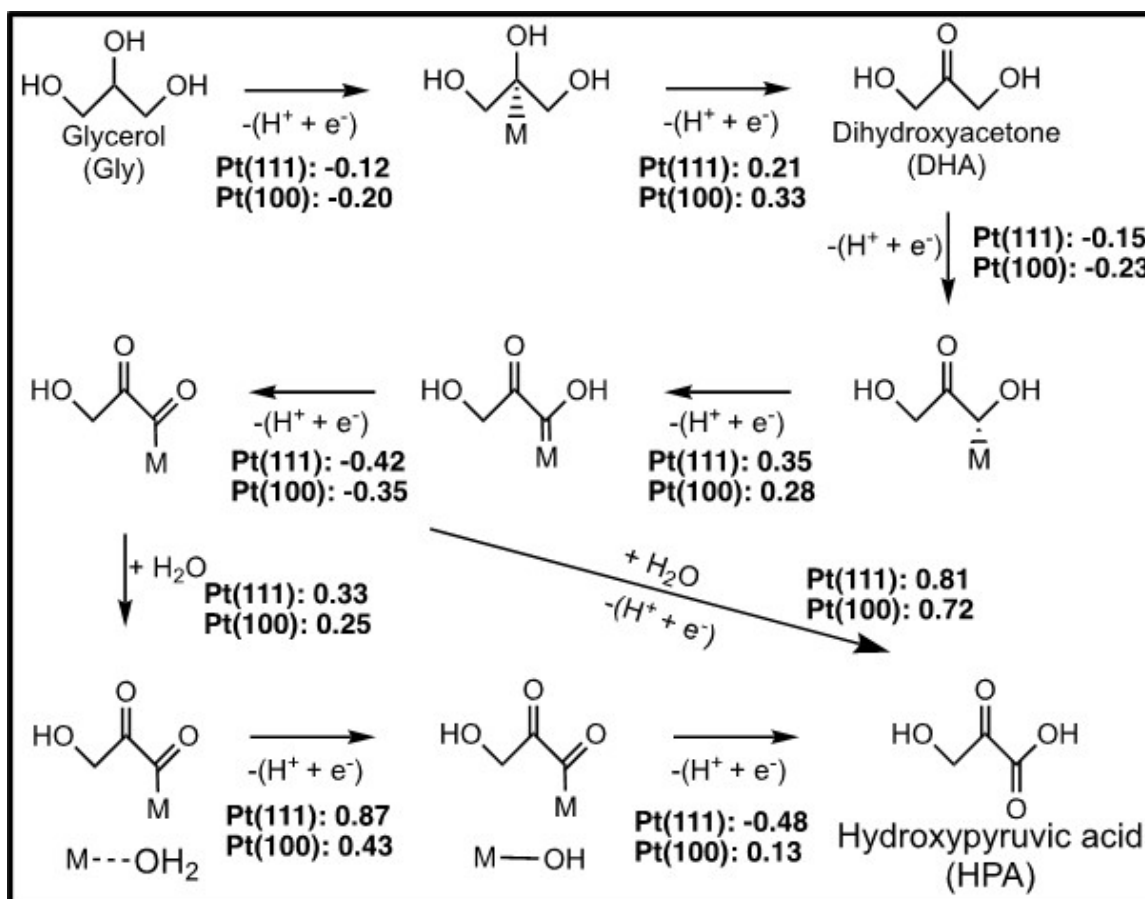
Figure S17: Illustration showing all the elementary steps and free energy differences for reactions **(1)** and **(1')** in figure 4. The letter "M" represents the closest site on the surface. Reaction energies are calculated as: $\Delta G_{Initial\ state} - \Delta G_{Final\ state}$. Here, free energies were calculated considering potential of 0 V vs. RHE. All the values are in eV.
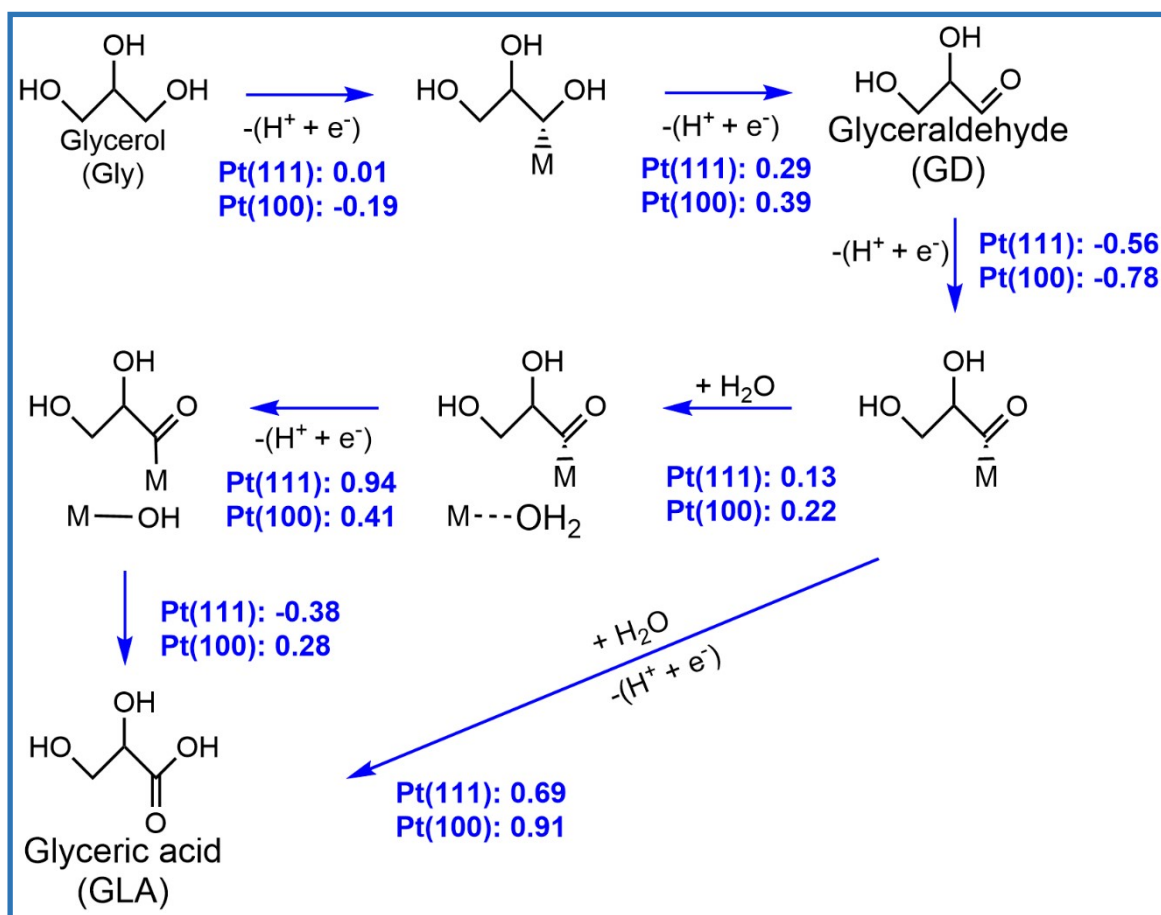
Figure S18: Illustration showing all the elementary steps and free energy differences for reaction **(2)** and **(2')** in figure 4. The letter "M" represents the closest site on the surface. Reaction energies are calculated as: $\Delta G_{Final\,state} - \Delta G_{Initial\,state}$. Here, free energies were calculated considering potential of 0 V vs. RHE. All the values are eV.

Figure S19: Illustration showing all the elementary steps and free energy differences for reaction **(3)** and **(3')** in figure 4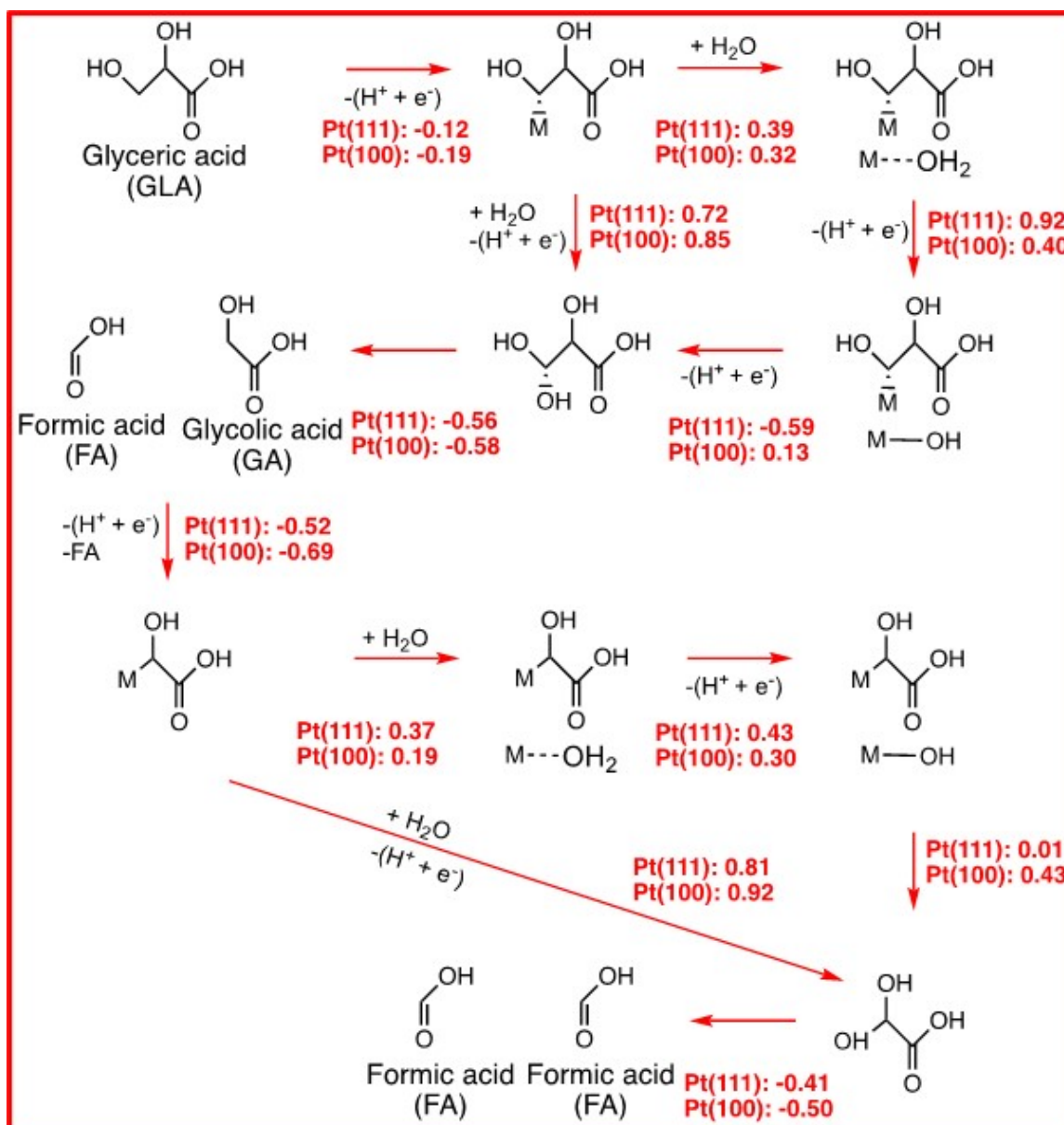. The letter "M" represents the closest site on the surface. Reaction energies are calculated as: $\Delta G_{Final\,state} - \Delta G_{Initial\,state}$. Here, free energies were calculated considering potential of 0 V vs. RHE. All the values are in eV.

Figure S20: Illustration showing all the elementary steps and free energy differences for reaction **(4)** and **(4')** in figure 4. The letter "M" represents the closest site on the surface. Reaction energies are calculated as: $\Delta G_{Final\,state} - \Delta G_{Initial\,state}$. Here, free energies were calculated considering potential of 0 V vs. RHE. All the values are in eV.
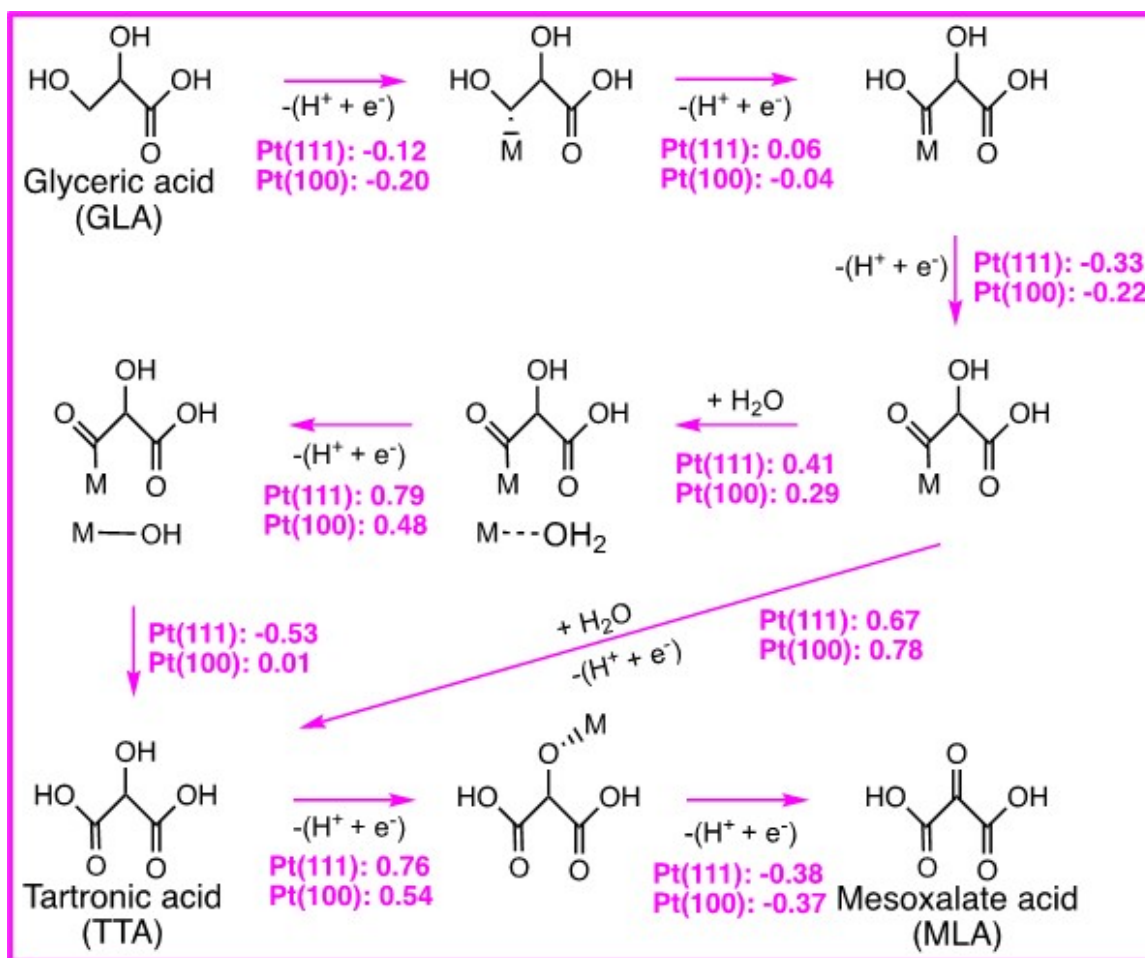
Figure S21: Illustration showing all the elementary steps and free energy differences for reaction **(5)** in figure 4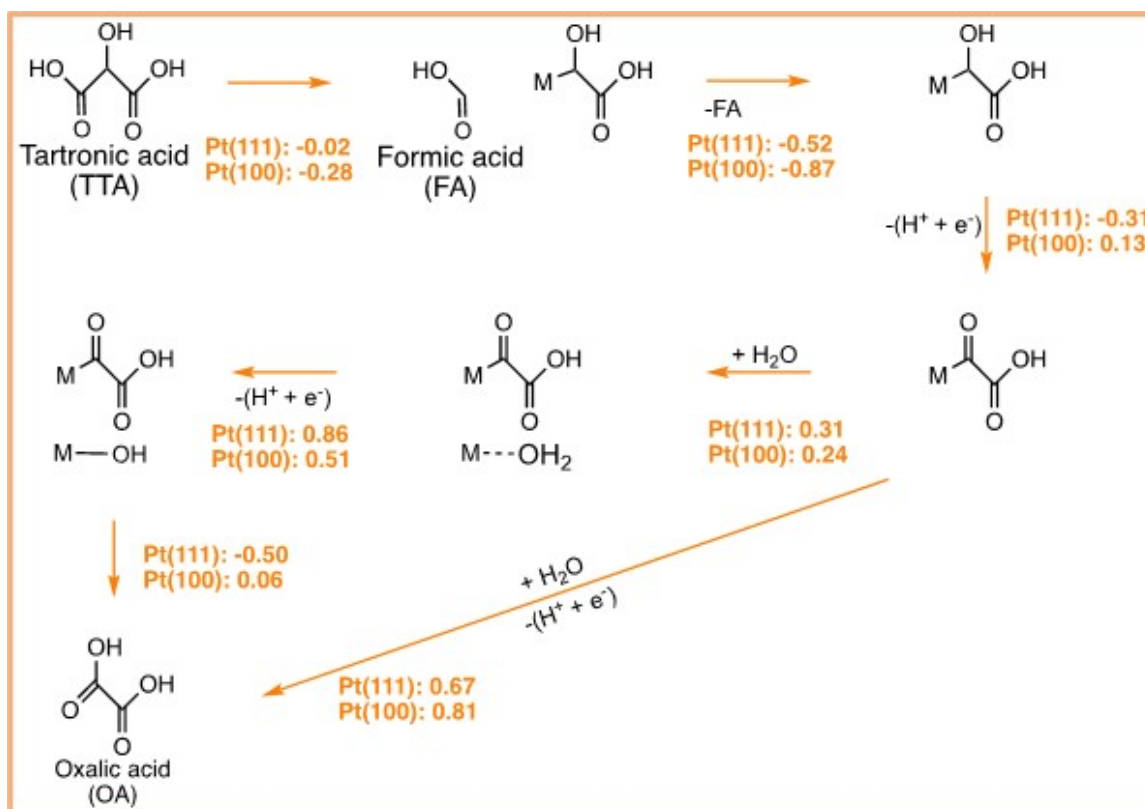. The letter "M" represents the closest site on the surface. Reaction energies are calculated as: $\Delta G_{Final\ state} - \Delta G_{Initial\ state}$. Here, free energies were calculated considering potential of 0 V vs. RHE. All the values are in eV.
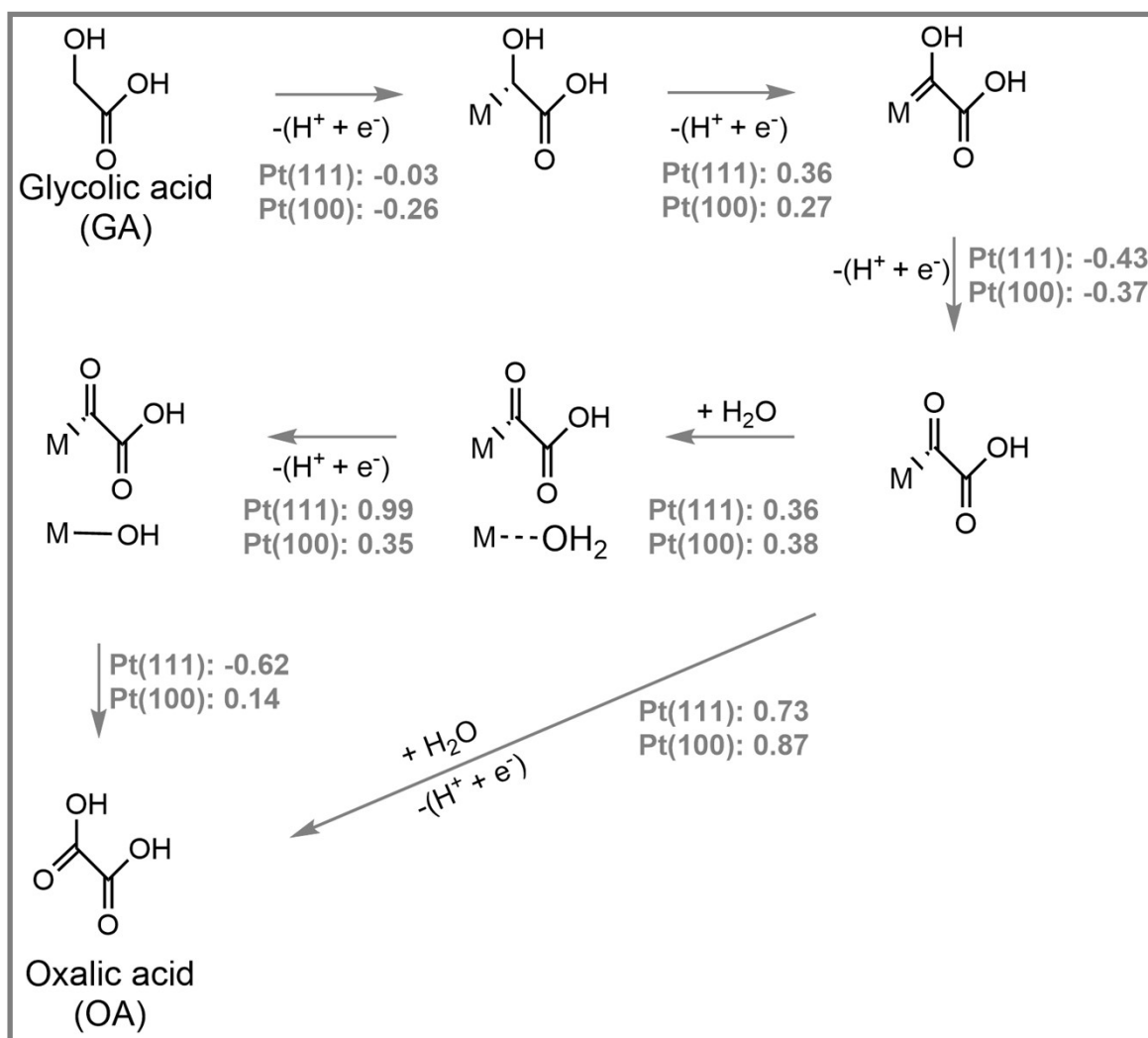
Figure S22: Illustration showing all the elementary steps and free energy differences difference for reaction **(6)** in figure 4. The letter "M" represents the closest site on the surface. Reaction energies are calculated as: $\Delta G_{Final\ state} - \Delta G_{Initial\ state}$. Here, free energies were calculated considering potential of 0 V vs. RHE. All the values are in eV.
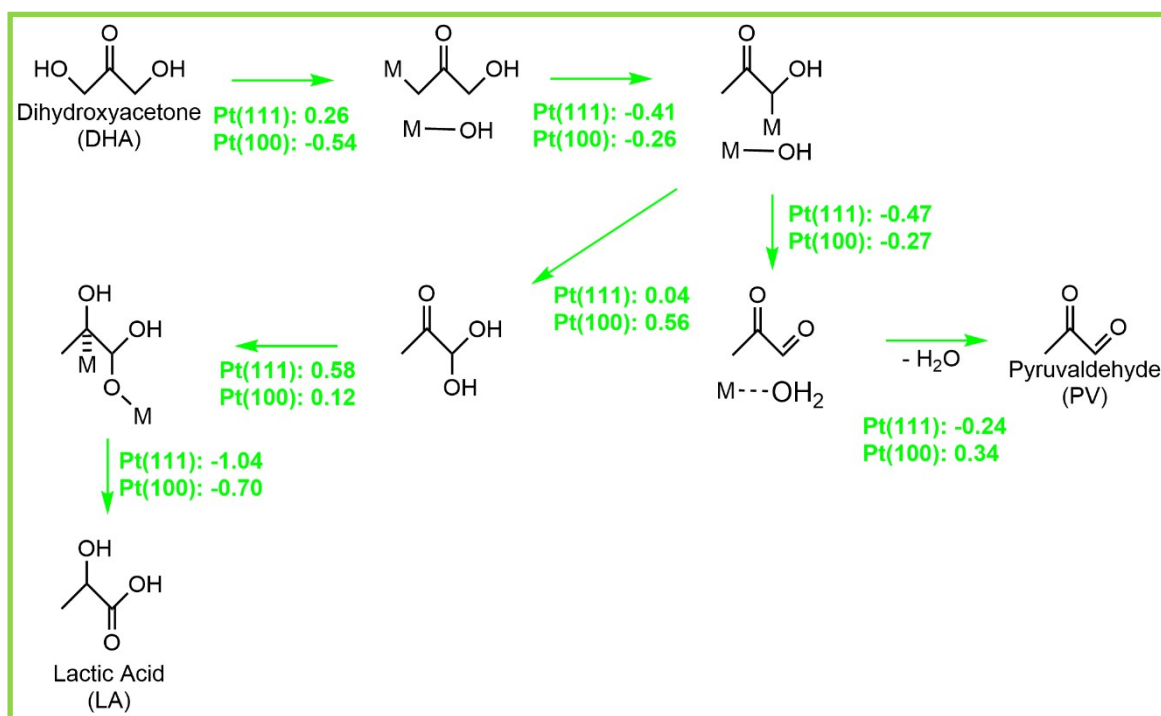
Figure S23: Illustration showing all the elementary steps and free energy difference for reaction **(7)** and **(7')** in figure 4. The letter "M" represents the closest site on the surface. Reaction energies are calculated as: $\Delta G_{Final\,state} - \Delta G_{Initial\,state}$. Here, free energies were calculated considering potential of 0 V vs. RHE. All the values are in eV.

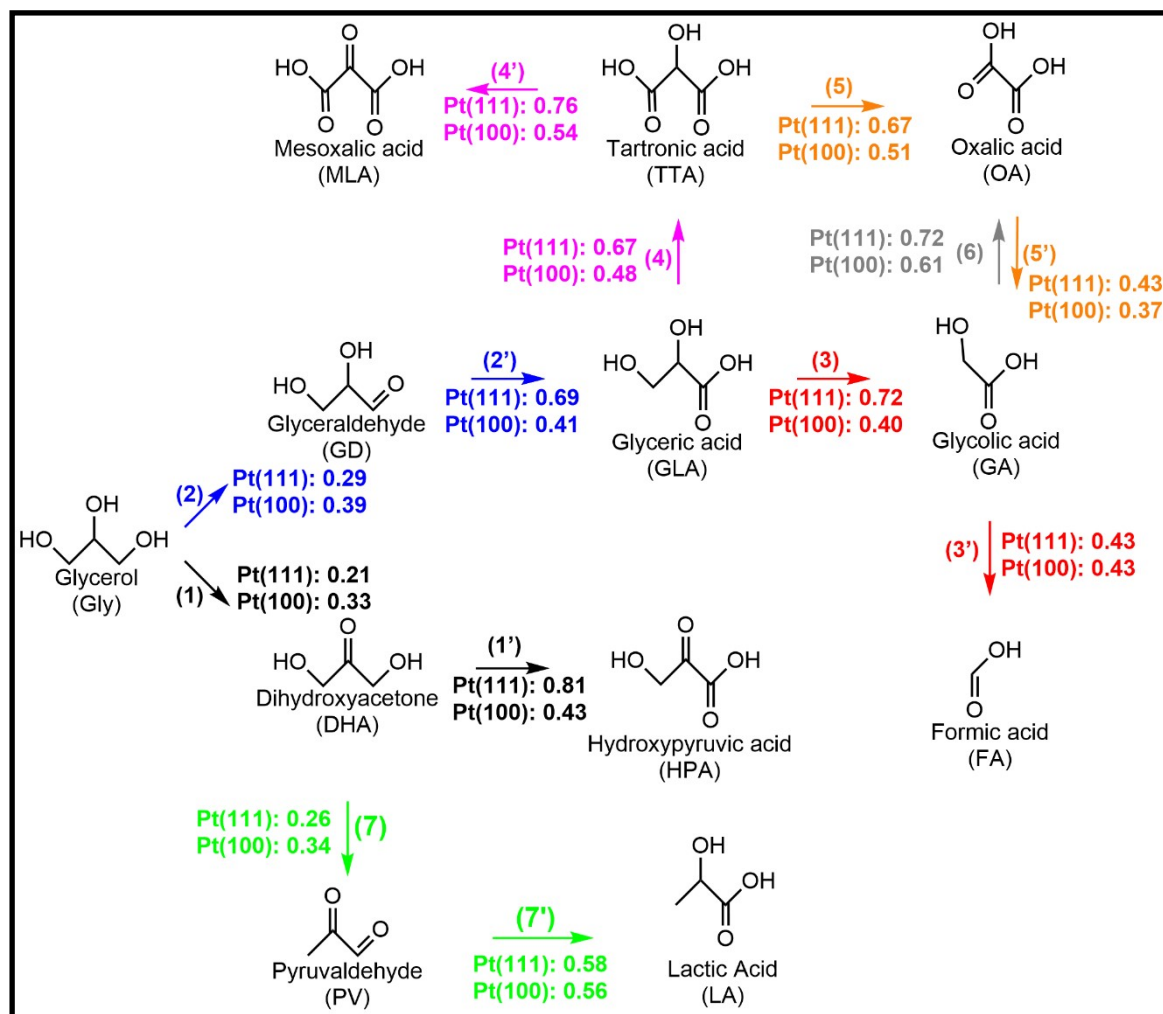## 4.3. Potential determining step of all liquid products

Figure S24: Illustration showing all the reactions considered in this work. Here the PDS (potential-determining step) values were calculated for both Pt (111) and Pt (100) surfaces based on **Figures S17-S23**.

Table S3: PDS values for the formation of all products starting from glycerol molecule. All values were obtained by analyzing **Figure S25**.

Pt (111)		Pt (100)	
DHA	0.21	DHA	0.33
PV	0.26	LA	0.34
GD	0.29	GD	0.39
LA	0.58	GA	0.40
GLA	**0.69**	**GLA**	**0.41**
TTA	0.69	PV	0.43
OA	0.69	HPA	0.43
GA	0.69	**FA**	**0.43**
FA	**0.69**	TTA	0.48
MLA	0.76	OA	0.51
HPA	0.81	MLA	0.54

4.4. Free energy step diagram
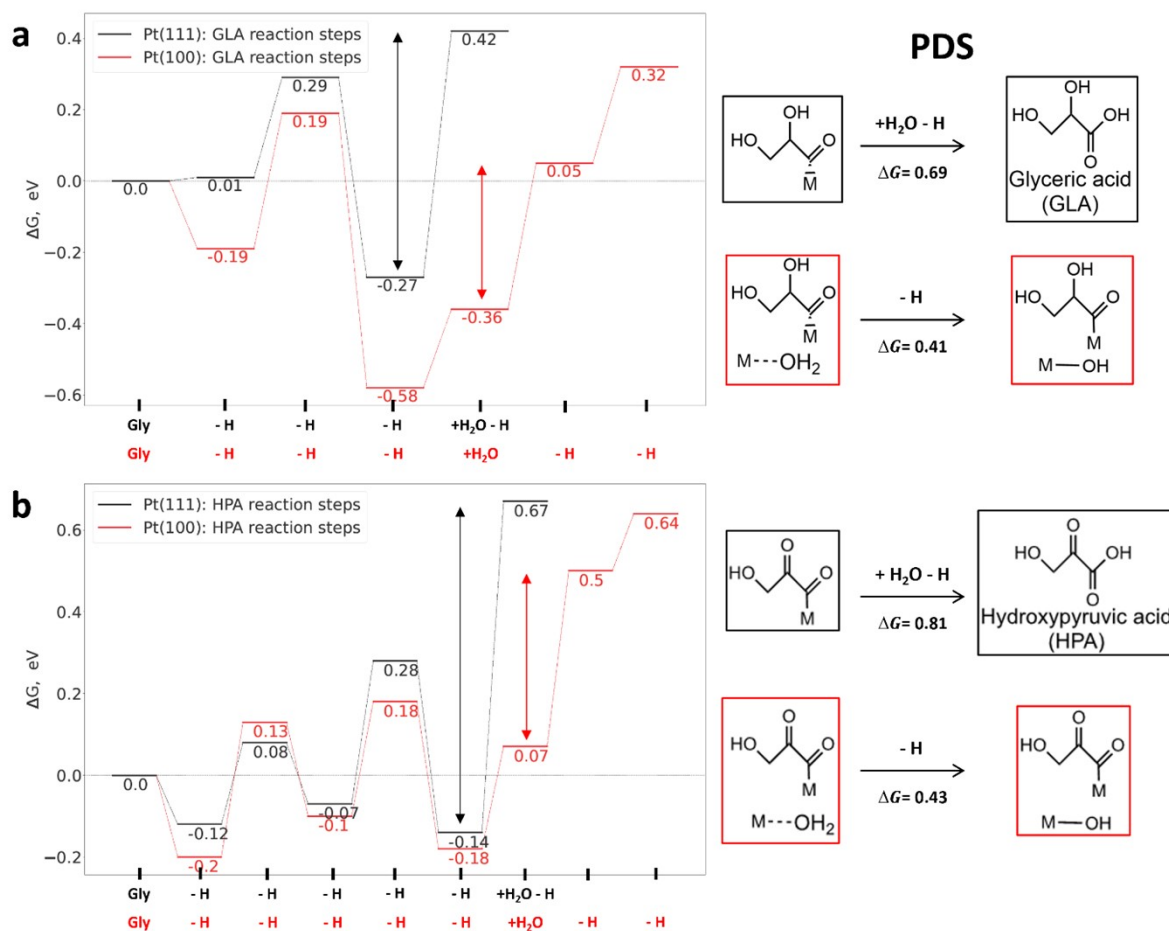
Figure S25: Free energy step diagram representing the formation of glyceric acid (GLA) and hydroxyl pyruvic acid (HPA) on Pt (111) and Pt (100) catalysts. The double-arrows represent the determinant reaction step, used to calculate PDS values. Inset downhill steps for GLA and HPA formation. This figure shows how PDS was calculated in Figure S17 and S18. Reaction energetics for all the reactions depicted in Figures 4 and S25 are shown in the Excel file, "Energetics_Pt111_Pt100.xlsx".

Supplementary References

1 K. Eiler, H. Krawiec, I. Kozina, J. Sort and E. Pellicer, *Electrochimica Acta*, 2020, **359**, 136952.

2 J. Ji, W. C. Cooper, D. B. Dreisinger and E. Peters, *J. Appl. Electrochem.*, 1995, **25**, 642–650.

3 S. Akbar, J. Boswell, S. Waters, S. Williams, J. M. Elliott and A. M. Squires, *ACS Appl. Nano Mater.*, 2021, **4**, 5717–5725.

4 S. J. Richardson, M. R. Burton, X. Luo, P. A. Staniec, I. S. Nandhakumar, N. J. Terrill, J. M. Elliott and A. M. Squires, *Nanoscale*, 2017, **9**, 10227–10232.

5 S. Akbar, J. M. Elliott, M. Rittman, A. M. Squires, S. Akbar, J. M. Elliott, A. M. Squires and M. R. Zbsa, *Adv. Mater.*, 2013, **25**, 1160–1164.

6 M. Łukaszewski, M. Soszko and A. Czerwiński, *Int J Electrochem Sci*, 2016, **11**, 4442–4469.

7 S. Trasatti and O. A. Petrii, *Pure Appl. Chem.*, 1991, **63**, 711–734.

8 K. Eiler, S. Suriñach, J. Sort and E. Pellicer, *Appl. Catal. B Environ.*, 2020, **265**, 118597.

9 J. S. Pedersen, *J. Appl. Crystallogr.*, 2000, **33**, 637–640.

10 S. Kerkhofs, T. Willhammar, H. Van, D. Noortgate, C. E. A. Kirschhock, E. Breynaert, G. Van Tendeloo, S. Bals and J. A. Martens, *Chem Mater*, 2015, **27**, 46.

11 V. Singh, P. Khullar, P. N. Dave and N. Kaur, *Int. J. Ind. Chem. 2013 41*, 2013, **4**, 1–18.

12 K. Eiler, H. Krawiec, I. Kozina, J. Sort and E. Pellicer, *Electrochimica Acta*, 2020, **359**, 136952.

13 Q. G. Zhang, B. Y. Cao, X. Zhang, M. Fujii and K. Takahashi, *J. Phys. Condens. Matter*, 2006, **18**, 7937.

14 Y. Cai and R. R. Adzic, *Adv Phys Chem*, 2011, 2011.

15 E. Westsson, S. Picken and G. Koper, *Chem. Commun.*, 2019, **55**, 1338–1341.

16 J. Li, P. Li, J. Li, Z. Tian and F. Yu, *Catalysts*, 2019, **9**, 506.

17 J. H. Kim, J. Y. Cheon, T. J. Shin, J. Y. Park and S. H. Joo, *Carbon*, 2016, **101**, 449–457.

18 S. Sharma, A. Ganguly, P. Papakonstantinou, X. Miao, M. Li, J. L. Hutchison, M. Delichatsios and S. Ukleja, *J. Phys. Chem. C*, 2010, **114**, 19459–19466.

19 **A. Falase**, M. Main, K. Garcia, A. Serov, C. Lau and P. Atanassov, *Electrochimica Acta*, 2012, **66**, 295–301.

20 Q. **Sun**, F. Gao, Y. Zhang, C. Wang, X. Zhu and Y. Du, *J. Colloid Interface Sci.*, 2019, **556**, 441–448.

21 L. Y. **Jiang**, A. J. Wang, X. S. Li, J. Yuan and J. J. Feng, *ChemElectroChem*, 2017, **4**, 2909–2914.

22 J. Han, Y. Kim, D. H. K. Jackson, H. Chang, H. W. Kim, J. Lee, J. R. Kim, Y. Noh, W. B. Kim, K. Y. Lee and H. J. Kim, *Appl. Catal. B Environ.*, 2020, **273**, 119037.

23 Y. **Zhou**, Y. Shen and J. Piao, *ChemElectroChem*, 2018, **5**, 1636–1643.

24 **Z. Zhang**, L. Xin and W. Li, *Appl. Catal. B Environ.*, 2012, **119–120**, 40–48.

25 E. **Ferreira** Frota, V. V. Silva de Barros, B. R. S. de Araújo, Â. Gonzaga Purgatto and J. J. Linares, *Int. J. Hydrog. Energy*, 2017, **42**, 23095–23106.

26 M. S. Ahmad, C. K. Cheng, S. Singh, H. R. Ong, H. Abdullah, C. S. Hong, G. K. Chua and M. R. Khan, *J. Nanosci. Nanotechnol.*, 2020, **20**, 5916–5927.

27 Y. Zhou, Y. Shen, X. Luo, G. Liu and Y. Cao, *Nanoscale Adv.*, 2020, **2**, 3423–3430.

28 Z. **Chen**, C. Liu, X. Zhao, H. Yan, J. Li, P. Lyu, Y. Du, S. Xi, K. Chi, X. Chi, H. Xu, X. Li, W. Fu, K. Leng, S. J. Pennycook, S. Wang and K. P. Loh, *Adv. Mater.*, 2019, **31**, 1804763.

29 X. Yu, E. C. dos Santos, J. White, G. Salazar-Alvarez, L. G. M. Pettersson, A. Cornell and M. Johnsson, *Small*, 2021, **17**, 2104288.

30 A. Hjorth Larsen, J. Jørgen Mortensen, J. Blomqvist, I. E. Castelli, R. Christensen, M. Dułak, J. Friis, M. N. Groves, B. Hammer, C. Hargus, E. D. Hermes, P. C. Jennings, P. Bjerre Jensen, J. Kermode, J. R. Kitchin, E. Leonhard Kolsbjerg, J. Kubal, K. Kaasbjerg, S. Lysgaard, J. Bergmann Maronsson, T. Maxson, T. Olsen, L. Pastewka, A. Peterson, C. Rostgaard, J. Schiøtz, O. Schütt, M. Strange, K. S. Thygesen, T. Vegge, L. Vilhelmsen, M. Walter, Z. Zeng and K. W. Jacobsen, *J Phys Condens Matter*, 2017, **29**, 273002.

31 G. Kresse and J. Furthmüller, *Phys. Rev. B*, 1996, **54**, 11169–11186.

32 J. Wellendorff, K. T. Lundgaard, A. Møgelhøj, V. Petzold, D. D. Landis, J. K. Nørskov, T. Bligaard and K. W. Jacobsen, *Phys. Rev. B*, 2012, **85**, 235149.

33 P. E. Blöchl, C. J. Först and J. Schimpl, *Bull. Mater. Sci. 2003 261*, 2003, **26**, 33–41.

34 D. R. Hamann, M. Schlüter and C. Chiang, *Phys. Rev. Lett.*, 1979, **43**, 1494–1497.

35 NIST-JANAF Thermochemical Tables, 4th Edition | NIST, https://www.nist.gov/publications/nist-janaf-thermochemical-tables-4th-edition, (accessed June 1, 2022).

36 J. K. Nørskov, J. Rossmeisl, A. Logadottir, L. Lindqvist, J. R. Kitchin, T. Bligaard and H. Jónsson, *J. Phys. Chem. B*, 2004, **108**, 17886–17892.

37 M. Fishman, H. L. Zhuang, K. Mathew, W. Dirschka and R. G. Hennig, *Phys. Rev. B*, 2013, **87**, 245402.

38 K. Mathew, R. Sundararaman, K. Letchworth-Weaver, T. A. Arias and R. G. Hennig, *J. Chem. Phys.*, 2014, **140**, 084106.